

The Magnetized Environment of the W3(H₂O) Protostars

Huei-Ru Chen^{1,2}, Ramprasad Rao², David J. Wilner³, and Sheng-Yuan Liu²

ABSTRACT

We present the first interferometric polarization map of the W3(OH) massive star-forming region observed with the Submillimeter Array (SMA) at 878 μm with an angular resolution of 1".5 (about 3×10^3 AU). Polarization is detected in the W3(H₂O) hot core, an extended emission structure in the north-west of W3(H₂O), and part of the W3(OH) ultracompact H II region. The W3(H₂O) hot core is known to be associated with a synchrotron jet along the east-west direction. In this core, the inferred magnetic field orientation is well aligned with the synchrotron jet and close to the plane of sky. Using the Chandrasekhar-Fermi method with the observed dispersion in polarization angle, we estimate a plane-of-sky magnetic field strength of 17.0 mG. Combined with water maser Zeeman measurements, the total magnetic field strength is estimated to be 17.1 mG, comparable to the field strength estimated from the synchrotron model. The magnetic field energy dominates over turbulence in this core. In addition, the depolarization effect is discerned in both SMA and JCMT measurements. Despite the great difference in angular resolutions and map extents, the polarization percentage shows a similar power-law dependence with the beam averaged column density. We suggest that the column density may be an important factor to consider when interpreting the depolarization effect.

Subject headings: ISM: individual (W3(H₂O)) — ISM: magnetic fields — Techniques: polarimetric — stars: formation

1. Introduction

One of the outstanding problems in star formation concerns the influence of magnetic fields to the dynamics and timescales (Shu et al. 1999; McKee & Ostriker 2007). The relative importance between magnetic fields and turbulence affects cloud evolution and cluster

¹Institute of Astronomy and Department of Physics, National Tsing Hua University, Hsinchu, Taiwan; hchen@phys.nthu.edu.tw.

²Institute of Astronomy and Astrophysics, Academia Sinica, Taipei, Taiwan.

³Harvard-Smithsonian Center for Astrophysics, Cambridge, MA.

formation (McKee & Ostriker 2007). Ambipolar diffusion has been proposed to regulate core collapse (Shu, Adams, & Lizano 1987). In accretion flows, magnetic effects such as magnetic tension, braking, and reconnection, or non-ideal magnetohydrodynamic (MHD) effects, can drive the evolution of the formation process (Shu, Li, & Allen 2004; Li, McKee, & Klein 2011). The residual magnetic fields in the circumstellar environs further assist to collimate supersonic outflows (Shu et al. 2000; Shang, Li, & Hirano 2007). Intriguingly, radio emission with negative spectral index has been reported in a few protostellar jets, e.g. HH80-81 (Martí, Rodríguez, & Reipurth 1993; Carrasco-Gonzalez et al. 2010), Cepheus A (Garay et al. 1996), W3(H₂O) (Reid et al. 1995; Wilner, Reid, & Menten 1999). Such non-thermal emission resembles jets driven by active galactic nuclei and suggests a connection with synchrotron jets.

It has become increasingly clear that dust grains are aligned by magnetic fields not only in the diffuse interstellar medium but also in dense cloud cores or circumstellar disks (Myers & Goodman 1991; Ward-Thompson et al. 2000; Lazarian, Goodman, & Myers 1997; Matthews et al. 2009; Dotson et al. 2000, 2010). Although grain alignment mechanisms may be less assured, polarization remains one of the most informative techniques to trace magnetic fields (Lazarian 2007). Complimentary to polarization from selective extinction of background starlight, polarized emission arising from magnetically aligned dust grains in the millimeter or submillimeter wavebands is often used to map the two-dimensional morphology of the three-dimensional (3D) magnetic fields projected on the plane of sky, B_{\perp} . Depending on the type of polarization, the observed orientation is supposed to be either parallel to B_{\perp} if observed in dust absorption against background sources or perpendicular to B_{\perp} if observed in dust thermal emission (see the review by Hildebrand 1988).

The bright ultracompact (UC) H II region, W3(OH), marks a nearby ($d = 2.04$ kpc; Hachisuka et al. 2006), well-studied massive star-forming region in the course of developing an OB stellar group. At least seven H II regions at different evolutionary stages were found within 30'' of W3(OH) (Harten 1976). The most recent star formation takes place in a luminous ($L \sim 10^4 L_{\odot}$) hot core, W3(H₂O) (a.k.a the Turner-Welch object), which is associated with water masers and appears as a warm, dense molecular clump about 6'' east to W3(OH) (Turner & Welch 1984). Millimeter and submillimeter interferometric studies resolved the dust emission into two components, A and C, and suggest an accreting proto-binary system (Wyrowski et al. 1999; Chen et al. 2006; Zapata et al. 2011). Proper motions of water masers trace a bipolar outflow centered at W3(H₂O)A (Alcolea et al. 1993; Hachisuka et al. 2006), which also drives a synchrotron jet along the east-west direction (Reid et al. 1995; Wilner et al. 1999). Here we perform interferometric polarization observations toward the W3(OH) massive star-forming region to map the morphology of the projected magnetic fields in this region. Our study is enabled by the Submillimeter Array⁴ (SMA) with its polarimeter

system (Marrone et al. 2006; Marrone & Rao 2008).

2. Observations and Data Reduction

Observations using quarter-wave plates installed on the SMA were carried out with seven antennas in the extended configuration on 2007 August 10 and with six antennas in the compact configuration on 2008 September 20. The phase tracking center is at $(\alpha, \delta)(\text{J2000}) = (2^{\text{h}}27^{\text{m}}3.870^{\text{s}}, +61^{\circ}52'24.60'')$. The system temperature varied from 150 to 580 K during the extended array observation and from 110 to 400 K during the compact array observation. The correlator was set to have a spectral resolution of 0.8125 MHz, corresponding to 0.7 km s^{-1} , and 2 GHz bandwidth in each sideband. The projected baselines have a range of 8 – 207 k λ , which is insensitive to structures larger than $11''$ (Wilner & Welch 1994). The full-width at half power (FWHP) of the primary beam is roughly $37''$.

Data inspection, calibration, and imaging were performed with the MIRIAD package. The instrumental polarization response, i.e. “leakage,” for each antenna was calibrated by observing strong quasars, 3c111 and 3c454.3, over a wide hour angle range for a good parallactic angle coverage. The bandpass calibration was performed with 3c454.3. Ganymede and Callisto were used to set the flux density scale, which is estimated to be accurate within 15%. Regularly interleaved observations of the nearby quasar 3c84 were conducted to monitor the atmospheric variations. Atmospheric complex gains were first solved with respect to 3c84 to make initial Stokes I images for individual tracks. The gain solutions were further improved by one iteration of phase-only self-calibration using the initial Stokes I images as models. To image continuum emission, care has been taken to remove channels with line emission. Both sidebands were used to generate line-free continuum maps in a multi-frequency synthesis with an effective central frequency of 341.5 GHz.

To obtain the best signal-to-noise ratio, maps of Stokes I (total intensity), and Stokes Q and U (linear polarization) were made with visibilities weighted by the associated system temperature using natural weighting. This results in a synthesized beam of $1''.4 \times 1''.5$ with position angle (P.A.) of -14° . For easy comprehension and convenience of subsequent Nyquist sampling, we smooth all the maps with a circular Gaussian beam of $1''.5$. The resultant maps have an rms noise level of $\sigma_I = 27 \text{ mJy beam}^{-1}$ for the Stokes I map and $\sigma_{QU} = 3 \text{ mJy beam}^{-1}$ for maps of Stokes Q and U . The dynamic range of the Stokes I map

⁴The Submillimeter Array is a joint project between the Smithsonian Astrophysical Observatory and the Academia Sinica Institute of Astronomy and Astrophysics, and is funded by the Smithsonian Institution and the Academia Sinica.

is limited at a maximum intensity value of $120\sigma_I$ due to the u - v coverage and calibration accuracy. Once Stokes I , Q , and U are known, the polarization percentage, p , and the polarization position angle, θ , can be deduced (Matthews & Wilson 2000). The raw polarized intensity, $I_{p,\text{raw}} = (Q^2 + U^2)^{1/2}$, is necessarily positive and biased by the rms noise of Stokes Q and U , σ_{QU} . Hence, a debiased polarized intensity is used, $I_p = (I_{p,\text{raw}}^2 - \sigma_{QU}^2)^{1/2}$ (Leahy 1989; Vaillancourt 2006) when computing the polarization percentage, $p = I_p/I$. The polarization position angle is determined by $\theta_{\text{obs}} = (1/2) \tan^{-1}(U/Q)$, with an uncertainty of $\sigma_{\theta,\text{obs}} = (1/2)(\sigma_{QU}/I_p)(180^\circ/\pi)$. Note that in linear polarization measurements, values of θ_{obs} different by 180° are identical. After generating maps of Stokes I , Q , and U , we image the distribution of polarization, including I_p , p , and θ_{obs} , for regions where $I_p \geq 3\sigma_{QU}$ and $I \geq 3\sigma_I$. Table 1 lists the Nyquist sampling of the polarization map with a grid step of $0''.75$.

3. Results and Discussion

The $878\ \mu\text{m}$ polarization map is shown in Figure 1. Line segments indicate the orientation of polarization angle, θ_{obs} , with their lengths proportional to the polarization percentage, p . Both the W3(H₂O) hot core and the W3(OH) UC H II region are clearly detected in the Stokes I map. Polarization is detected in W3(H₂O), W3(OH), and their vicinity, particularly in a faint, extended component in the north-west of W3(H₂O). In the W3(OH) UC H II region, the total intensity is dominated by the free-free continuum, which is supposed to be unpolarized. Additional care is needed to estimate the relative contributions from dust and free-free emission to the total intensity in W3(OH), and this will be discussed elsewhere.

3.1. Morphology and Properties of Detected Polarization

In Table 1, we group the detected polarization values based on their apparent association with distinct polarization subregions: W3(H₂O), W3(H₂O)-NW referring to the extended structure in the north-west of W3(H₂O), W3(H₂O)-E and W3(H₂O)-W referring to the two small regions in the east and west of W3(H₂O), respectively. With the exception of W3(H₂O)-NW, there is a general east-west orientation of B_\perp across the whole region (Figure 2).

In W3(H₂O), the polarization orientation is remarkably uniform, $\theta_{\text{obs}} = -12^\circ - 20^\circ$. The mean polarization angle weighted by observational uncertainty is $\langle\theta_{\text{obs}}\rangle = 0^\circ \pm 2^\circ$. We compute the standard deviation, $\delta\theta_{\text{obs}}$, with respect to $\langle\theta_{\text{obs}}\rangle$ and obtain a value of 11.4° (Table 2). This observed dispersion, $\delta\theta_{\text{obs}}$, includes the measurement uncertainty, which is the root mean square (rms), $\delta\sigma_{\theta,\text{obs}}$, of the observed uncertainties, $\sigma_{\theta,\text{obs}}$. Hence, the intrinsic

dispersion of polarization angle is given by $\delta\theta = (\delta\theta_{\text{obs}}^2 - \delta\sigma_{\theta,\text{obs}}^2)^{1/2} = 9.4^\circ$ and will be used to estimate the magnetic field strength of B_\perp (Sect. 3.2). In addition, the distribution of polarization angle in W3(H₂O)-NW (Figure 1) also appears fairly uniform. We compute for W3(H₂O)-NW a mean polarization angle of $\langle\theta_{\text{obs}}\rangle = 54^\circ \pm 2^\circ$ and an intrinsic polarization angle dispersion of $\delta\theta = 10.2^\circ$.

3.2. The Magnetized Environment of the Synchrotron Jet in W3(H₂O)

The synchrotron jet exhibits a double-sided morphology along the east-west direction centered at the millimeter continuum peak W3(H₂O)A in the VLA 3.6 cm map (Figure 2; Wilner et al. 1999). Our uncertainty weighted mean polarization angle of $\langle\theta_{\text{obs}}\rangle = 0^\circ \pm 2^\circ$ implies an east-west orientation of B_\perp , in good agreement with the direction of the synchrotron jet. In early VLA studies of the synchrotron jet (Reid et al. 1995; Wilner et al. 1999), an inhomogeneous model of a biconical geometry with opening angle of 0.1 rad successfully reproduced the observed properties. The model gave a total magnetic field strength of $B(r) = 10 \text{ mG } (r/0''.2)^{-0.8}$, where r is the angular distance from the center.

The field strength of the projected magnetic field component, B_\perp , can be estimated if the dispersion of the polarization angle, $\delta\theta$, the mass density, ρ , and the velocity dispersion along line of sight, δv_{los} , are measured. Considering a uniform magnetic field, Chandrasekhar & Fermi (1953; hereafter CF) first proposed a ‘‘polarization-dispersion’’ method to estimate B_\perp based on transverse motions of Alfvén waves, which are observable as dispersion in polarization angles, $\delta\theta$, from the mean orientation of the projected fields. If the velocity dispersion is isotropic and the transverse velocity dispersion is equal to δv_{los} , one can obtain the plane-of-sky magnetic field strength

$$\begin{aligned} B_\perp &= Q \sqrt{4\pi\rho} \frac{\delta v_{\text{los}}}{\delta\theta} \\ &= 68.6 \text{ mG} \left(\frac{Q}{0.5}\right) \left(\frac{\mu}{1.36}\right)^{1/2} \left(\frac{n_{\text{H}_2}}{10^7 \text{ cm}^{-3}}\right)^{1/2} \left(\frac{\delta v_{\text{los}}}{1 \text{ km s}^{-1}}\right) \left(\frac{\delta\theta}{1^\circ}\right)^{-1}, \end{aligned} \quad (1)$$

where $Q = 1$ corresponds to the original CF formula, and μ is the mean molecular weight. In a later study, Ostriker, Stone, & Gammie (2001) performed 3D numerical MHD simulations with conditions in turbulent clouds and suggested a factor of $Q \sim 0.5$ applicable at varying observer orientations as long as $\delta\theta \lesssim 25^\circ$. Chen et al. (2006) have studied the physical conditions in W3(H₂O) by analyzing the 1.4 mm and 2.8 mm continuum and the CH₃CN lines. Since our polarization observations do not resolve individual protostellar envelopes, we simply take their mean value of $n_{\text{H}_2} = 1.5 \times 10^7 \text{ cm}^{-3}$ and $\delta v_{\text{los}} = 1.9 \text{ km s}^{-1}$ based on the CH₃CN spectra. Using Equation (1), we estimate the magnetic field strength to be

$B_{\perp} = 17.0$ mG. Since $\delta\theta_{\text{obs}}$ can be lowered by the finite angular resolution and averaging along line of sight, this estimate of B_{\perp} should be considered as an upper limit.

When Zeeman measurements are available to provide the line-of-sight magnetic field strength, B_{\parallel} , it is possible to evaluate the total field strength with $B = (B_{\perp}^2 + B_{\parallel}^2)^{1/2}$. This offers an independent method to estimate the total field strength in comparison with the synchrotron model. The Zeeman measurements in 22 GHz H₂O masers in W3(H₂O) yield a postshock field strength of $B_{\parallel,\text{post}} = +42.1$ mG (Sarma et al. 2002). Depending on the degree of shock compression, the field could be amplified by a factor of about 20 (Sarma et al. 2002) and renders an estimate for the preshock field strength of $B_{\parallel} = +2.1$ mG. Hence, an estimate of the total field strength is about $B \simeq 17.1$ mG, with orientation close to the plane of sky. Though slightly higher, this total field strength is comparable to the value given by the synchrotron model (Reid et al. 1995; Wilner et al. 1999).

Following Crutcher (1999), we estimate the observed-to-critical mass-to-magnetic flux ratio, $(M/\Phi_B)_{\text{obs/crit}} = (N_{\text{H}_2}/10^{24} \text{ cm}^{-2})/(B/10 \text{ mG}) = 0.54$, for W3(H₂O) with $N_{\text{H}_2} = 9.2 \times 10^{23} \text{ cm}^{-2}$ (Chen et al. 2006). This implies the core is magnetically subcritical and can be supported by the static magnetic field against the gravitational collapse. However, ongoing collapse in this region has been suggested by infall asymmetry in spectral profiles (Wu & Evans 2003; Wu et al. 2010). Since interferometric observations tend to underestimate column density and B_{\perp} is an upper limit, our estimate of $(M/\Phi_B)_{\text{obs/crit}}$ should be treated as a lower limit. Using the total field strength, the Alfvén velocity is given by $v_A = B/(4\pi\rho)^{1/2} = 4.2 \text{ km s}^{-1}(B/10 \text{ mG})(n_{\text{H}_2}/10^7 \text{ cm}^{-3})^{-1/2} = 5.9 \text{ km s}^{-1}$. The ratio of the turbulent to magnetic energy can be evaluated with $\beta_{\text{turb}} = 3(\delta v_{\text{los}}/v_A)^2 = 0.31$, implying that the magnetic energy dominates over turbulence in this hot core (Girart et al. 2009).

Unlike the hot core, there are very limited observations addressing the extended structure W3(H₂O)-NW. We are not able to estimate the field strength for B_{\perp} at the moment. The mean polarization angle of $\langle\theta_{\text{obs}}\rangle = 54^{\circ} \pm 2^{\circ}$ in this extended structure appears quite different from the general north-south polarization orientation and implies B_{\perp} to be at P.A. = -36° . Based on its morphology and relative position with W3(OH) and the northern H II region (Figure 2), we speculate that W3(H₂O)-NW could be residual matter being pushed by the expansion of the northern H II region and the champagne flow from W3(OH).

3.3. Comparison with Polarization Measurements on Large Scales

Our polarization measurements show a decrease of polarization percentage, p , toward regions of higher intensity, I , (Figure 3a, black dots). To avoid complication caused by the

UC H II region, we exclude polarization measurements in W3(OH). Assuming a power-law dependence, we obtain a relationship of $\log p = (-0.73 \pm 0.05) \log I + (0.30 \pm 0.02)$ with a reduced chi-square of $\overline{\chi^2} = 2.2$. This “depolarization” phenomenon has been reported in many regions, e.g. L1755 (Lazarian et al. 1997), Orion-KL (Rao et al. 1998), OMC-3 (Matthews, Wilson, & Fiege 2001), W51 (Lai, Girart, & Crutcher 2003; Tang et al. 2009b), G5.89–0.39 (Tang et al. 2009a). The reduction of polarization may be due to complexity of magnetic field geometry (Matthews et al. 2001), decreasing dust alignment efficiency (Lazarian et al. 1997), beam smearing over small-scale structures (Rao et al. 1998), and integration of varying magnetic domains along the line of sight.

The SMA polarization measurements nicely fill in the central polarization “hole” in the larger scale 850 μm polarization map from the James Clerk Maxwell Telescope (JCMT) of Matthews et al. (2009). The three innermost JCMT measurements sit around the edge of the 37'' SMA field of view. In addition, the JCMT measurements with an angular resolution of 20'' also show the depolarization effect (Figure 3a; gray triangles). Despite the great difference in angular resolutions and map extents between the SMA and JCMT observations, the JCMT measurements yield a similar relationship of $\log p = (-0.72 \pm 0.05) \log I + (1.05 \pm 0.03)$ with $\overline{\chi^2} = 1.1$. To understand this similarity, we convert the dust intensity to column density with assumptions of a gas-to-dust mass ratio of 100, a dust opacity of $\kappa_\nu = 10 (\lambda/250 \mu\text{m})^{-\beta} \text{cm}^2 \text{g}^{-1}$ (Hildebrand 1983), and a dust temperature of 20 and 105 K for the JCMT and SMA measurements, respectively (Wilson, Gaume, & Johnston 1993; Wink et al. 1994). For the central region, we derived $\beta = 0.9$ by comparing the flux density between 2.8 mm (Chen et al. 2006) and 878 μm in maps made with visibilities of projected baselines within 8 – 207 $k\lambda$, the range that the two frequencies have in common. Such small β is often attributed to grain growth in high-density environment (Miyake & Nakagawa 1993) and is not valid in the outer region. To convert the JCMT measurements, we adopt $\beta = 1.6$ for active protostellar cores (Rathborne et al. 2010). In Figure 3b, the polarization percentage shows a similar dependence with the beam averaged column density between the two populations of polarization measurements (Figure 3b). A fit using all the data gives $\log p = (-0.72 \pm 0.02) \log N_{\text{H}_2} + (17.7 \pm 0.6)$ with $\overline{\chi^2} = 1.4$. We suggest that the column density may be an important factor when interpreting the depolarization effects caused by decreasing alignment efficiency, beam smearing, and integration along line of sight.

4. Summary

We present the first interferometric polarization map in the W3(OH) massive star-forming region observed with the SMA at 878 μm with an angular resolution of 1''.5, corre-

sponding to 3×10^3 AU. The main findings are summarized as follows:

1. The magnetic field orientation is well aligned with the synchrotron jet in W3(H₂O) and is close to the plane of sky with $B_{\perp} = 17.0$ mG. The total field strength is estimated to be 17.1 mG, slightly higher but comparable to the estimate of 10 mG from the synchrotron model. The magnetic energy dominates over turbulence in the hot core.
2. The depolarization effect is discerned in both the SMA and JCMT measurements. We find that the polarization percentage has a similar power-law dependence with the beam averaged column density for the two populations of polarization measurements. The column density may be an important factor to consider when interpreting the depolarization effect caused by decreasing alignment efficiency, beam smearing, and integration along line of sight.
3. The extended emission structure in the north-west of W3(H₂O) has a significant polarization detection that suggests the B_{\perp} orientation at P.A. = -36° .

This research is supported by National Science Council of Taiwan through grant NSC 100-2112-M-007-004-MY2. Vivien Chen would like to thank Dr. B. Matthews for the general guideline to convert JCMT SCUPOL flux density.

REFERENCES

- Alcolea, J., Menten, K. M., Moran, J. M., & Reid, M. J. 1993, in Proc. Conf. Astrophysical Masers, Vol. 412, Lecture Notes in Physics, ed. A. W. Clegg & G. E. Nedoluha (Berlin: Springer-Verlag), 225
- Carrasco-Gonzalez, C., Rodriguez, L. F., Anglada, G., Martí, J., Torrelles, J. M., & Osorio, M. 2010, *Science*, 330, 1209
- Chandrasekhar, S. & Fermi, E. 1953, *ApJ*, 118, 113
- Chen, H.-R., Welch, W. J., Wilner, D. J., & Sutton, E. C. 2006, *ApJ*, 639, 975
- Crutcher, R. M. 1999, *ApJ*, 520, 706
- Dotson, J. L., Davidson, J., Dowell, C. D., Schleuning, D. A., & Hildebrand, R. H. 2000, *ApJS*, 128, 335

- Dotson, J. L., Vaillancourt, J. E., Kirby, L., Dowell, C. D., Hildebrand, R. H., & Davidson, J. A. 2010, *ApJS*, 186, 406
- Garay, G., Ramirez, S., Rodriguez, L. F., Curiel, S., & Torrelles, J. M. 1996, *ApJ*, 459, 193
- Girart, J. M., Beltrán, M. T., Zhang, Q., Rao, R., & Estalella, R. 2009, *Science*, 324, 1408
- Hachisuka, K., Brunthaler, A., Menten, K. M., Reid, M. J., Imai, H., Hagiwara, Y., Miyoshi, M., Horiuchi, S., et al. 2006, *ApJ*, 645, 337
- Harten, R. H. 1976, *A&A*, 46, 109
- Hildebrand, R. H. 1983, *QJRAS*, 24, 267
- Hildebrand, R. H. 1988, *MNRAS*, 29, 327
- Lai, S.-P., Girart, J. M., & Crutcher, R. M. 2003, *ApJ*, 598, 392
- Lazarian, A. 2007, *Journal of Quantitative Spectroscopy & Radiative Transfer*, 106, 225
- Lazarian, A., Goodman, A. A., & Myers, P. C. 1997, *ApJ*, 490, 273
- Leahy, P. 1989, *VLA Scientific Memorandum*, 161
- Li, P. S., McKee, C. F., & Klein, R. I. 2011, *ApJ*, 744, 73
- Marrone, D. P., Moran, J. M., Zhao, J.-H., & Rao, R. P. 2006, *ApJ*, 640, 308
- Marrone, D. P., & Rao, R. 2008, in *Proc. SPIE 7020, Millimeter and Submillimeter Detectors and Instrumentation for Astronomy IV*, ed. W. D. Duncan et al. (Bellingham, WA: SPIE), 60
- Martí, J., Rodriguez, L. F., & Reipurth, B. 1993, *ApJ*, 416, 208
- Matthews, B. C., McPhee, C. A., Fissel, L. M., & Curran, R. L. 2009, *ApJS*, 182, 143
- Matthews, B. C. & Wilson, C. D. 2000, *ApJ*, 531, 868
- Matthews, B. C., Wilson, C. D., & Fiege, J. D. 2001, *ApJ*, 562, 400
- McKee, C. F. & Ostriker, E. C. 2007, *ARA&A*, 45, 565
- Miyake, K., & Nakagawa, Y. 1993, *Icarus*, 106, 20
- Myers, P. C. & Goodman, A. A. 1991, *ApJ*, 373, 509

- Ostriker, E. C., Stone, J. M., & Gammie, C. F. 2001, *ApJ*, 546, 980
- Rathborne, J. M., Jackson, J. M., Chambers, E. T., Stojimirovic, I., Simon, R., Shipman, R., & Frieswijk, W. 2010, *ApJ*, 715, 310
- Rao, R., Crutcher, R. M., Plambeck, R. L., & Wright, M. C. H. 1998, *ApJ*, 502, L75
- Reid, M. J., Argon, A. L., Masson, C. R., Menten, K. M., & Moran, J. M. 1995, *ApJ*, 443, 238
- Sarma, A. P., Troland, T. H., Crutcher, R. M., & Roberts, D. A. 2002, *ApJ*, 580, 928
- Shang, H., Li, Z.-Y., & Hirano, N. 2007, in *Protostars and Planets V*, ed. B. Reipurth, D. Jewitt, & K. Keil (Tucson, AZ: Univ. Arizona Press), 261
- Shu, F. H., Adams, F. C., & Lizano, S. 1987, *ARA&A*, 25, 23
- Shu, F. H., Allen, A., Shang, H., Ostriker, E. C., & Li, Z.-Y. 1999, in *The Origin of Stars and Planetary Systems*, ed. C. J. Lada & N. D. Kylafis (Dordrecht: Kluwer), 193
- Shu, F. H., Li, Z.-Y., & Allen, A. 2004, *ApJ*, 601, 930
- Shu, F. H., Najita, J. R., Shang, H., & Li, Z.-Y. 2000, in *Protostars and Planets IV*, ed. V. Mannings, A. P. Boss, & S. S. Russell (Tucson, AZ: Univ. Arizona Press), 789
- Tang, Y.-W., Ho, P. T. P., Girart, J. M., Rao, R., Koch, P., & Lai, S.-P. 2009a, *ApJ*, 695, 1399
- Tang, Y.-W., Ho, P. T. P., Koch, P. M., Girart, J. M., Lai, S.-P., & Rao, R. 2009b, *ApJ*, 700, 251
- Turner, J. L. & Welch, W. J. 1984, *ApJ*, 287, L81
- Vaillancourt, J. E. 2006, *PASP*, 118, 1340
- Ward-Thompson, D., Kirk, J. M., Crutcher, R. M., Greaves, J. S., Holland, W. S., & André, P. 2000, *ApJ*, 537, L135
- Wilner, D. J., Reid, M. J., & Menten, K. M. 1999, *ApJ*, 513, 775
- Wilner, D. J. & Welch, W. J. 1994, *ApJ*, 427, 898
- Wilson, T. L., Gaume, R. A., & Johnston, K. J. 1993, *ApJ*, 402, 230

- Wink, J. E., Duvert, G., Guilloteau, S., Gusten, R., Walmsley, C. M., & Wilson, T. L. 1994, *A&A*, 281, 505
- Wu, J. & Evans, N. J. 2003, *ApJ*, 592, L79
- Wu, J., Evans, N. J., Shirley, Y. L., & Knez, C. 2010, *ApJS*, 188, 313
- Wyrowski, F., Schilke, P., Walmsley, C. M., & Menten, K. M. 1999, *ApJ*, 514, L43
- Zapata, L. A., Rodríguez-Garza, C., Rodríguez, L. F., Girart, J. M., & Chen, H.-R. 2011, *ApJ*, 740, L19

Table 1. Polarization measurements at 878 μm

R.A. Offset ^a (arcsec)	Decl. Offset ^a (arcsec)	I^b (Jy beam ⁻¹)	p (%)	$\theta_{\text{obs}} \pm \sigma_{\theta, \text{obs}}$ (deg)	Remarks
W3(H ₂ O)					
4.53	-0.59	1.36	1.0 ± 0.2	-12 ± 7	
5.28	-0.59	1.96	0.7 ± 0.2	-2 ± 7	
4.53	0.16	2.37	1.1 ± 0.1	-3 ± 4	
5.28	0.16	3.20	1.2 ± 0.1	-2 ± 2	I_p peak
6.03	0.16	2.60	0.8 ± 0.1	0 ± 5	
3.78	0.91	1.10	0.9 ± 0.3	19 ± 10	
4.53	0.91	2.06	0.7 ± 0.2	20 ± 7	
5.28	0.91	2.48	0.7 ± 0.1	5 ± 5	
6.03	0.91	1.86	0.7 ± 0.2	10 ± 7	
W3(H ₂ O)-NW					
3.78	1.66	0.83	2.6 ± 0.4	47 ± 4	
4.53	1.66	0.99	2.1 ± 0.3	59 ± 5	
3.03	2.41	0.30	3.9 ± 1.2	32 ± 8	
3.78	2.41	0.42	4.3 ± 0.8	53 ± 5	
4.53	2.41	0.39	5.6 ± 0.9	64 ± 4	
3.03	3.16	0.08	17.0 ± 6.8	44 ± 7	
3.78	3.16	0.12	11.1 ± 3.6	53 ± 7	
4.53	3.16	0.10	10.6 ± 4.6	70 ± 9	
W3(H ₂ O)-E and W3(H ₂ O)-W					
9.78	-0.59	0.14	7.4 ± 2.8	23 ± 9	W3(H ₂ O)-E
2.28	0.16	0.10	12.3 ± 4.9	-29 ± 8	
3.03	0.16	0.25	4.1 ± 1.4	-31 ± 9	
2.28	0.91	0.26	4.2 ± 1.4	-3 ± 9	
3.03	0.91	0.53	1.8 ± 0.6	3 ± 10	
W3(OH) without free-free continuum subtraction					
-0.72	-1.34	0.38	2.5 ± 0.9	-75 ± 10	
0.03	-1.34	0.35	3.3 ± 1.0	-79 ± 8	
-0.72	-0.59	1.24	1.4 ± 0.3	-74 ± 5	
0.03	-0.59	1.27	1.5 ± 0.3	-73 ± 5	

Table 1—Continued

R.A. Offset ^a (arcsec)	Decl. Offset ^a (arcsec)	I^b (Jy beam ⁻¹)	p (%)	$\theta_{\text{obs}} \pm \sigma_{\theta, \text{obs}}$ (deg)	Remarks
0.78	-0.59	0.54	1.8 ± 0.6	-70 ± 10	
-0.72	0.16	1.81	0.6 ± 0.2	-75 ± 9	
0.03	0.16	1.98	0.7 ± 0.2	-68 ± 7	
0.03	1.66	0.38	2.6 ± 0.9	1 ± 9	
0.78	1.66	0.23	4.2 ± 1.5	9 ± 10	

^aPosition offsets with respect to the map center at $(\alpha, \delta)(\text{J2000}) = (2^{\text{h}}27^{\text{m}}3.870^{\text{s}}, +61^{\circ}52'24.60'')$.

^bThe rms of the Stokes I map is $0.027 \text{ Jy beam}^{-1}$.

Table 2. Dispersions of Polarization Angles

Region	$\langle \theta_{\text{obs}} \rangle$ (deg)	$\delta \theta_{\text{obs}}$ (deg)	$\delta \sigma_{\theta, \text{obs}}$ (deg)	$\delta \theta$ (deg)	n_{H_2} (10^7 cm^{-3})	δv_{los} (km s^{-1})	B_{\perp} (mG)
W3(H ₂ O)	0 ± 2	11.4	6.4	9.4	1.5	1.90	17.0
W3(H ₂ O)-NW	54 ± 2	12.0	6.4	10.2

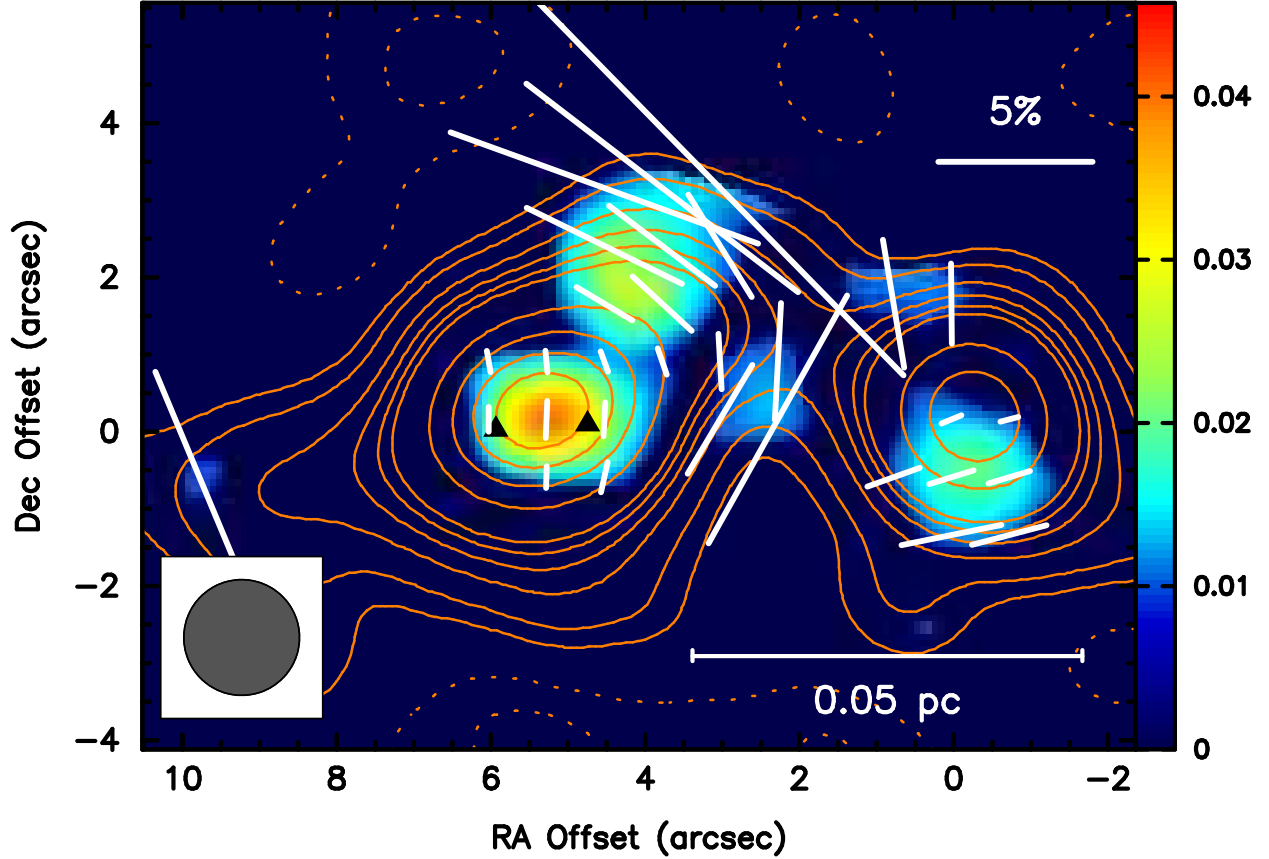


Fig. 1.— Polarization map of the W3(OH) region at $878 \mu\text{m}$ with the total intensity (Stokes I) map (contours) overlaid on the linearly polarized intensity, I_p , map (colors). Line segments give polarization orientation with their lengths proportional to the polarization percentage and are plotted where $I_p \geq 3\sigma_{QU}$ and $I \geq 3\sigma_I$. The rms value is $\sigma_I = 27 \text{ mJy beam}^{-1}$ for the Stokes I map and $\sigma_{QU} = 3 \text{ mJy beam}^{-1}$ for maps of Stokes Q and U . In the total intensity map, the western clump is the W3(OH) UC H II region while the eastern clump is the W3(H₂O) hot core, where triangles mark the two 1.4 mm continuum peaks, A and C, from east to west. Two distinct and uniform distributions of polarized emission are observed in W3(H₂O) and W3(H₂O)-NW. Note that the total intensity in W3(OH) is complicated by the free-free continuum of the UC H II region. Additional care is required to derive the polarization measurements. Contour levels correspond to $(-4, -2, 2, 4, 8, 12, 16, 20, 40, 60, 80) \times \sigma_I$. The angular resolution is $1''.5$.

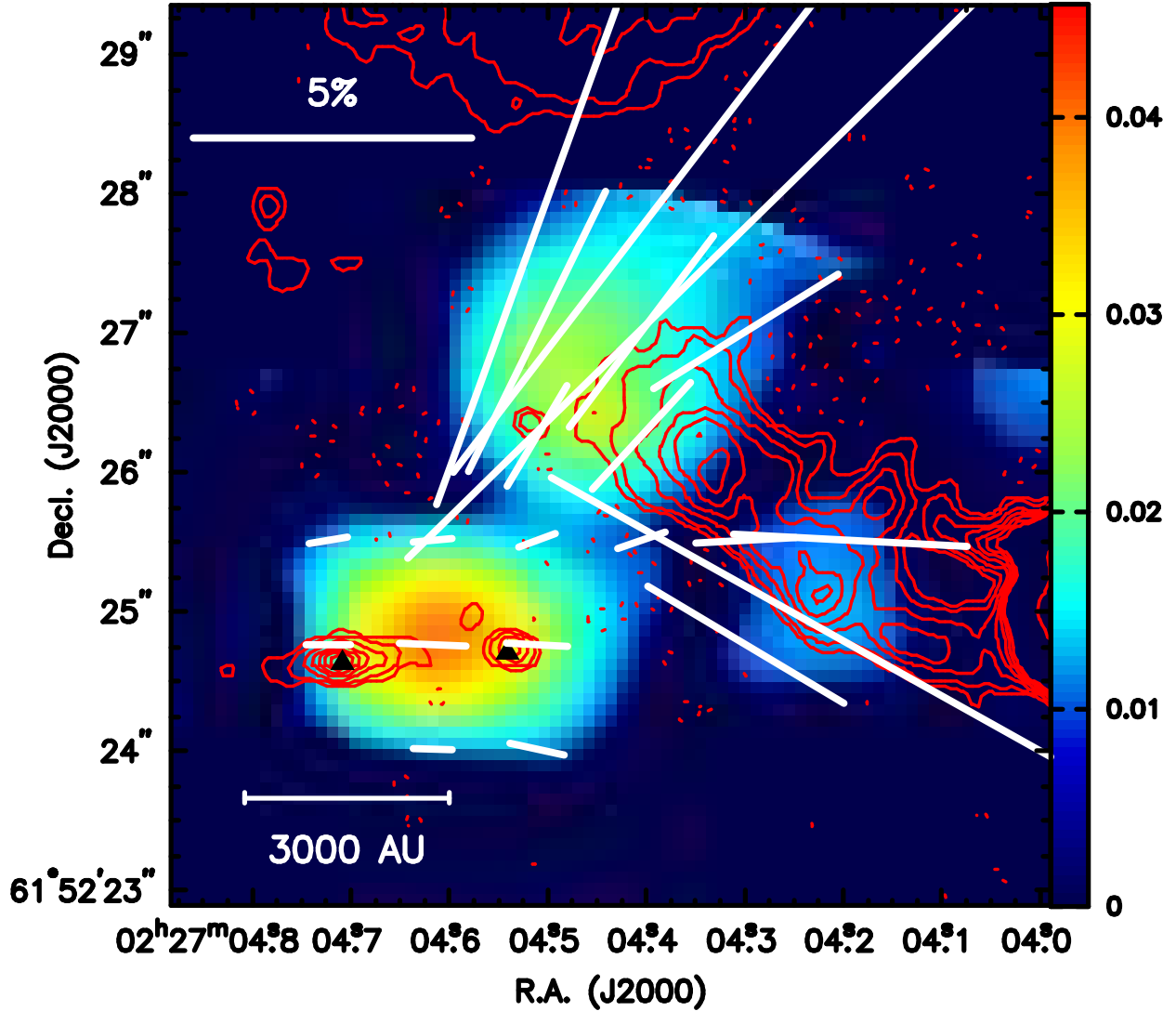


Fig. 2.— The VLA 3.6 cm continuum map (contours; Wilner et al. 1999) overlaid on the 878 μm linearly polarized intensity, I_p , map (colors). Line segments represent the inferred orientation of the projected magnetic fields, B_{\perp} . Triangles mark the two 1.4 mm continuum peaks in W3(H₂O), where the eastern peak, W3(H₂O)A, is associated with the synchrotron jet seen in the VLA 3.6 cm map. Contour levels correspond to 30, 60, 120, 180, 240, 300, 360, 500 $\mu\text{Jy beam}^{-1}$.

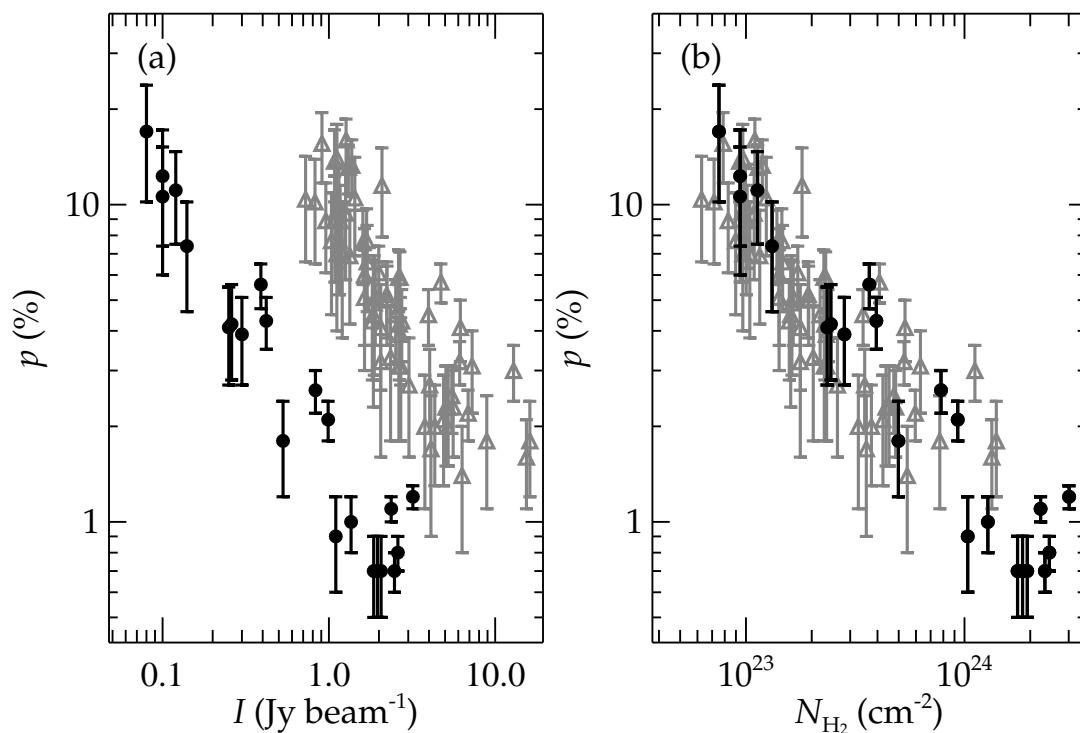


Fig. 3.— (a) Polarization percentage, p , vs. total intensity, I . Black dots are polarization measurements with the SMA whereas the gray triangles are measurements with the JCMT. (b) Polarization percentage, p , vs. beam-averaged column density, N_{H_2} . Despite the great difference in angular resolutions and map extents between the SMA and JCMT observations, a similar dependence is found with the beam averaged column density.